A multimodal microcharacterization of trace-element zonation and Running head: multimodal characterization of zonation in cassiterite

Guillaume Wille, Catherine Lerouge, Schmidt Ute

A multimodal microcharacterization of trace-element zonation and crystallographic orientation in natural cassiterite by combining cathodoluminescence, EBSD, EPMA and contribution of confocal Raman-in-SEM imaging

Running head: multimodal characterization of zonation in cassiterite

WILLE Guillaume [1]*, LEROUGE Catherine [1], SCHMIDT Ute [2]

[1] BRGM, 3 Avenue Claude Guillemin, BP 36009, 45060 ORLEANS Cedex 2, FRANCE

[2] WITec GmbH, Lise-Meitner-Straße 6, 89081 Ulm, GERMANY

*Corresponding author: g.wille@brgm.fr / phone +33 (0)238643522 / fax +33 (0)238643711

ABSTRACT

In cassiterite, tin is associated with metals (titanium, niobium, tantalum, indium, tungsten, iron, manganese, mercury). Knowledge of mineral chemistry and trace-element distribution is essential for: the understanding of ore formation, the exploration phase, the feasibility of ore treatment, and disposal/treatment of tailings after the exploitation phase. However, the availability of analytical methods make these characterizations difficult.

We present a multi-technical approach to chemical and structural data that includes scanning electron microscopy (SEM)-based imaging and microanalysis techniques such as : secondary and backscattered electrons, cathodoluminescence (CL),

Electron Probe Microanalyzer (EPMA), Electron Backscattered Diffraction (EBSD) and confocal Raman-imaging integrated in a SEM (RISE). The presented results show the complementarity of the used analytical techniques. SEM, CL, EBSD, EPMA provide information from the interaction of an electron beam with minerals, leading to atomistic information about their composition, whereas RISE, Raman spectroscopy and imaging completes the studies with information about molecular vibrations, which are sensitive to structural modifications of the minerals. The correlation of Raman bands with the presence/absence of Nb, Ta, Fe (heterovalent substitution), and Ti (homovalent substitution) is established at a sub-micrometric scale. Combination of the different techniques makes it possible to establish a direct link between chemical and crystallographic data of cassiterite.

KEYWORDS

Cassiterite, SEM, cathodoluminescence, EBSD, EPMA, Raman-in-SEM, RISE

SECOND ABSTRACT – LAY DESCRIPTION

Tin is a metal that has been used commercially since the Bronze Age. Cassiterite (SnO_2), a natural tin oxide, has been the most important source of tin (Sn) since that time. Sn is also associated with other metals such as titanium (Ti), niobium (Nb), tantalum (Ta), indium (In), tungsten (W), iron (Fe), manganese (Mn), mercury (Hg) in cassiterite. A thorough knowledge of its mineral chemistry and trace element distribution is necessary in the exploration phase for a better understanding of ore formation, for ore treatment feasibility, and for the disposal of tailings after the exploitation phase. However, these characterizations remain a challenge due to numerous analytical insufficiencies.

This paper presents a complementary multi-technical approach to chemical and structural data using a panel of imaging and microanalytical techniques based on scanning electron microscopy (SEM), chemical imaging, cathodoluminescence in the SEM (SEM-CL - internal structure, trace element distribution), electron probe micro-analysis (EPMA – chemical analysis and imaging at the micrometric scale), electron backscattered diffraction (EBSD – crystallographic mapping) and RISE confocal Raman-in-SEM imaging (chemical imaging). The correlation of SEM-CL intensity with crystallographic orientation (EBSD) and trace element distribution (EPMA) can clearly be established and the influence of each element on luminescence intensity can be defined at the micrometric scale.

In addition, the benefits of using the RISE microscope are highlighted. The analyses of the same areas of cassiterite grains show the complementarity of the different analyses and observations performed by SEM-CL imaging, crystallographic observations (EBSD), elemental analyses and trace elements distribution (EPMA), and confocal Raman spectroscopy and imaging in the SEM (RISE). The correlation of A_n and B_{2G} Raman bands with the presence/absence of trace elements Nb, Ta, Fe (heterovalent substitution) and Ti (homovalent substitution) is established at a sub-micrometric scale. The combination of data collected from the different techniques makes it possible to link directly both chemical and crystallographic data of cassiterite.

INTRODUCTION

Cassiterite (SnO_2) has been and continues to be the most important source of tin (Sn). Sn is also associated with other metals such as titanium (Ti), niobium (Nb), tantalum (Ta), indium (In), and tungsten (W), which can complicate ore treatment,

although some of these metals can be extracted as by-products. A detailed knowledge of mineral chemistry and trace element distribution is necessary in the exploration phase for: a better understanding of ore formation, ore treatment feasibility, and tailings disposal after the exploitation phase.

Cassiterite crystallizes in the tetragonal system with a space group of D41h4- P 4 /mnm. Because of its rutile-type structure, cassiterite can incorporate significant amounts of Ti, and also trace elements. Similar to rutile, natural cassiterite can incorporate Fe, Mn, Nb, Ta, In, W, and Hg (Botelho & Moura, 1998; Briskey, 2005; Cerny et al., 1985; Giuliani, 1987; Izoret et al., 1985; Lerouge et al., 2007; Möller et al., 1988; Murciego et al., 1997 ; Neiva, 1996 ; Serranti et al., 2002). Characterization of cassiterite remains a challenge for analytical techniques. EPMA is lacking due to interference of Sn and trace elements. X-ray emission lines of In Lα, Ta Mα in wavelength-dispersive X-ray spectroscopy (WDS) can only be solved by the use of less intense bands (Ta Mβ or Lα for example). SEM is required due to the nanometric size of the zonation areas, however, the BSE detector is often not sensitive enough for the detection of the low content of trace elements. Cathodoluminescence in the SEM however reveals the trace elements distribution.

Raman spectroscopy measures the vibrational frequencies of molecular bonds in a material. The resulting Raman spectrum is not only unique for a given compound, but is also sensitive to the local environment. The spectrum reveals structural data; it provides details on the chemical and structural properties (nature of the functional groups, symmetry group, lattice defects, etc…) and the crystallinity of mineral compounds. This method offers a variety of analytical possibilities that include, among others, identification of different polymorphs (Hope et al., 2001, Gao et al., 2009), determination of different oxidation states (Das & Hendry, 2011) and

crystallographic orientations (Mossbrucker & Grotjohn, 1996), evaluation of temperature (Lahfid et al., 2010) and stress effects on crystal and molecular structure (Mossbrucker & Grotjohn, 1997).

The availability of Raman spectroscopy in a SEM equipped with imaging detector (Secondary electrons (SE), backscattered electrons (BSE), cathodoluminescence (CL), ...), and microcharacterization (EDS, WDS, EBSD) allows morphological, elemental, chemical, and physical studies without transferring the sample from one instrument to another. Commercial systems have been available for about 15 years. These systems use an “on-axis” configuration, i.e. a parabolic mirror is inserted under the pole piece of the SEM to carry the laser beam to the sample surface and to collect diffused light for spectroscopic analysis (Wille et al., 2014). The mirror is connected through a special interface to a conventional µ-Raman spectrometer. The advantage of such a system has been established for different applications, including forensic applications (Otieno-Alego, 2009) and characterization of individual particles (Worobiec et al., 2010; Stefaniak et al., 2014), biological samples (Jarvis & Goodacre, 2004; Jarvis et al., 2004), and mineralogical samples (Stefaniak et al., 2009; Maubec et al., 2013).

Another Raman-in-SEM configuration has been proposed (Van Apeldoorn et al., 2005) and a commercial version is available, but it is affected by several limitations (in particular, a limited spectral range). A similar configuration, named “RISE” (Raman Imaging and Scanning Electron microscopy) has been developed by manufacturers Tescan (SEM) and Witec (Raman) and major improvements have been proposed to address the former on-axis configuration (Jiruse et al., 2014). This new configuration, which can be defined as a “parallel setup,” entails the use of a precise stage and an image repositioning tool to transfer the sample in the SEM

chamber from an SEM position (under the pole piece) to a Raman position (under the Raman objective). Unlike the “on-axis” setup, the parallel setup makes it possible to collect Raman spectra without any intensity loss compared to a conventional µ-Raman equipped with the same optical objective. Moreover, Raman mapping is possible through the collection of a “data cube” (one spectrum collected for each pixel of the optical image) at high speed (Jiruse et al., 2014).

For this study, Cassiterite from the Cadomian Montbelleux Sn ±W ore deposit has been selected because of the millimetric- to centimetric-size and the euhedral forms of the crystals, its high concentrations of rare metals including Nb, Ta, Fe, Ti, In and W, and strong chemical zoning compared to cassiterite from Variscan Sn ore deposits in Brittany, French Massif Central and Galicia (Lerouge et al., 2017). The substitutions in rare metals were discussed, but their distribution remains unknown at the crystal scale. This paper presents a complementary multi-technical approach to chemical and structural data that was tested on cassiterite crystal specimens from Montbelleux to provide a better characterization of chemical zoning; the approach includes scanning electron microscopy (SEM), cathodoluminescence in-SEM imaging (CL), electron probe micro-analysis (EPMA), electron backscattered diffraction (EBSD).

The contribution and features introduced by coupling SEM and Raman spectroscopy in a coupled SEM-confocal micro-Raman imaging and spectroscopy (RISE) are highlighted.

MATERIAL AND METHODS

Materials

Montbelleux is located at Luitré (Ille-et-Vilaine, France) in the Cadomian belt of northern Brittany, and more precisely in the Mancellian Domain (Ballèvre et al., 2001)

(Figure 1). Mineralization occurs as quartz-cassiterite-wolframite stockwork in a greisen topaz-bearing sodic granite dated at 490 ± 15 Ma by Rb-Sr isochron (Rossi et al., 1988) and as quartz-wolframite veins in schist at the contact with the batholith (Chauris et al., 1989). Cassiterite from greisen granite, previously analysed for trace elements using EPMA, is rich in Fe, Nb, Ta, Ti, compared to other Variscan Sn deposits in Brittany (Lerouge et al., 2017) (Table 1). Additionally the morphology of the crystals is of significant interest. Such samples, containing millimetric cassiterite grains, were selected and prepared as polished sections for mineralogical investigations (Figure 2).

Methods

Electron beam microscopy and microcharacterization techniques

Polished sections were observed in the SEM, under low vacuum conditions (uncoated samples) for EBSD and RISE and high vacuum conditions (carbon-coated samples) for CL and EPMA. Elemental mapping and quantitative analyses were performed using EPMA on carbon-coated polished sections. Carbon-coated polished sections were coated with 20 nm carbon using a Cressington 308 (Cressington, Watford, UK).

SEM images were obtained using a Tescan Mira 3 XMU (Tescan, Brno, Czech Republic) equipped with a secondary electron (SE) Everhart-Thornley detector (Everhart & Thornley, 1960) for high vacuum SE imaging, a low vacuum (LV) SE detector (Jacka et al., 2003) for LV – SE imaging and a YAG-scintillator backscattered electron (BSE) detector (Autrata-type BSE detector - Autrata, 1992) at HV = 25 kV and a panchromatic cathodoluminescence detector (350 – 650 nm)

(TESCAN BSE/CL detector). Low vacuum mode (LV) was used, with P = 20 Pa nitrogen.

Orientation maps were obtained using an Edax Pegasus system with a Digiview IV camera and OIM DC 6.4 software (Edax, Mahwah, USA). Collection was done on non-coated samples at HV = 25 kV, under low vacuum conditions (P=20 Pa Nitrogen). Samples had been previously polished using a high quality protocol including a colloidal silica final step.

Wavelength-dispersive X-ray spectroscopy (WDS) elemental mapping was performed on a Cameca SXFive electron microprobe (Cameca, Gennevilliers, France) using an accelerating voltage of 20 kV and a beam current of 200 nA. Complementary spot analyses were performed using an accelerating voltage of 20 kV and intensity of 50 nA to quantify the amount of Nb, Ta, Ti, Fe, and W. Ti Kα, Sn Lα, Nb Lα were measured on PET (pentaerythritol, 2d = 8.74Å), Fe Kα, on LiF (Lithium fluoride, 2d = 4.0267 Å) and Ta Mβ, W Lα on TAP (thallium acid phtalate, 2d = 25.75 Å). Counting time was 10 s for Ti, Fe, and Mn and 40 s for the other elements. Standards of calibration for EPMA spot quantitative analyses are natural minerals: cassiterite for Sn, synthetic oxides: $MnTiO_3$ for Ti and Fe2O3 for Fe, and pure elements: Nb, Ta and W metals. The detection limits of the elements for a single analysis, given in $mg.kg^{-1}$, are for Ti, Fe, Sn, Ta, In and Nb in table 1.

<u>RISE Raman imaging in the SEM</u>

Informations on the local chemistry of zoned cassiterite can be obtained at a submicrometric scale using Confocal Raman spectroscopy and Imaging. Confocal Raman imaging was performed on a Tescan-Witec RISE microscope combining a Tescan Mira SEM integrated with a Witec Confocal Raman Imaging System (Witec,

Ulm, Germany). The RISE confocal Raman imaging system is equipped with a UHTS300 spectrometer, a Zeiss 100x vacuum objective (N.A. 0.75) mounted inside the SEM chamber, using a 532 nm laser excitation wavelength (Jiruse et al., 2014).

RESULTS AND DISCUSSION

Zonation and crystal orientation in cassiterite grains using SE, CL, EBSD, and EPMA

Cassiterite has been extensively studied with cathodoluminescence (CL) to elucidate processes of crystal growth (Farmer et al., 1991). CL imaging of a centimetric cassiterite grain from Montbelleux, acquired in SEM, provides evidence of intense contrast variations (Figure 2). These contrasts can be attributed to very fine chemical zoning in trace elements (Hall & Ribbe, 1971; Remond, 1973; Remond et al., 1992) and to crystal orientations which are known to strongly affect cathodoluminescence in cassiterite (Hall, 1978).

To decrypt the origin of the CL contrast, a small area highlighted with the red arrow in Figure 2 (figure 3) was analyzed with various techniques. Figure 4 shows the EBSD inverse pole figure (IPF) map (Figure 4a) the corresponding CL image (Figure 4b) and the inverse pole figure projection (Figure 4c), acquired from an area of 253x190 μm^2. The EBSD IPF map was collected with a step of 1 µm. A cleaning procedure (grain dilation) was applied to remove mis-indexed points. The CL and EBSD images show identical contrasts. Both images show the presence of cracks, the only topographic features on a polished surface. The change of grey in the SE image (figure 2) corresponds to an orientation contrast due to electron channelling, a phenomenon that occurs in a crystal due to the interaction between primary electrons and the crystal structure (Lloyd, 1987). A similar change is observed also in the

EBSD image, providing evidence of mono-oriented grains with twinning. Twinning is well known in cassiterite as the “elbow twin” (Nespolo & Souvignier, 2015). An orientation variation of 68° was measured between the twin and the main orientation of the centimetric grain (Figure 4a), which is close to 70°, the ideal structure (Nespolo & Souvignier, 2015).

The CL image (Figure 4b) shows in addition the presence of alternating dark and bright bands which are associated with chemical zoning due to the incorporation of trace elements.

A comparison of the three images in Figure 4 reveals that the alternating bands in the CL image are parallel to the crystal faces and change their orientation in the corresponding twin crystals.

Trace element mapping was conducted by EPMA. EPMA trace element analysis is challenging due to the existence of interferences between the detectable trace elements. For example, tantalum (Ta), an element detected in this cassiterite grain, can be analyzed on the Mα line, which has the highest intensity at HV = 15 – 30 kV. However, interference occurs between Ta Mα and Sn $L\alpha^{(2nd\ order)}$ peaks on a TAP monochromator (Figure 5). The use of the differential mode is a good opportunity to remove the contribution of this Sn $L\alpha^{(2nd\ order)}$ peak when the differential mode window is set to 3 V. A small contribution is still evident (about 1.5 x background level in SnO_2). A further reduction of the whidth of the differential mode window (lower than 800 mV) is not able to completely remove the 2^{nd} order contribution. It leads to a greatly reduced peak intensity, which can be detrimental for trace analysis. As a result, Ta was collected on Ta Lα at 8.145 KeV. These results are presented in table 2, where only detected elements are reported.

Elemental mapping was performed by EPMA (WDS spectrometers) on the same area than CI and EBSD. Experimental conditions were determined to highlight trace element distribution. Elemental maps were collected at HV = 20 kV and beam current = 200 nA, map resolution = 512x512 pixels (stage scanning, step = 1 µm). Like CL image, elemental mapping of trace elements provides evidence of complex chemical zoning of Nb, Ti, Ta, and Fe. EPMA (WDS) maps (peak intensity) for Ta, Nb, Fe and Ti are presented in Figure 6 (figure 6 c to f) and compared with SEM-CL and RISE images obtained from the same sample area.The main zonation domains are surrounded by white lines to highlight the correspondence between trace element distribution, CL contrast and Raman spectral variations. According to table 2, Ti is the most abundant trace element and is regularly distributed in large Ti-rich bands alternating with fine Ti-poor bands corresponding to crystal growth. Nb and Fe are less abundant with the same order of content, according to EPMA analyses. On the contrary, Nb is more heterogeneously distributed throughout the cassiterite crystal (figure 6d), with irregular domains that are chemically zoned and highly enriched in Nb, and other crystal domains that are not clearly zoned and are poorer in Nb. The distribution of these domains compared to the EBSD map (figure 5) also provides evidence of a line probably corresponding to the limit of the twinning. Ta is present at very low concentrations (table 2). Comparison of the different elemental maps indicates that some rare Ta-rich bands seem to correspond to Nb-rich bands, and Ti-depleted bands to Fe-rich bands.

The cathodoluminescence properties of cassiterite depend to a great degree on trace elements content (Farmer et al., 1991; Hall & Ribbe, 1971; Remond, 1973). The CL image of the mapped area confirms the relationship between crystal growth and trace element distribution (figure 6). However, the relationship between trace element

distribution and luminescence is complex. The Fe-rich zones seem to correspond to very low luminescence, and luminescence is quenched when Ti is associated with Fe.

Ti acts as an activator, whereas luminescence is quenched when Fe is present with Ti. The influence of Ti on the CL activation is shown in various places in this area. Furthermore, Nb and Ta may turn out to have a negative effect on the panchromatic cathodoluminescence intensity. However, in numerous places in the observed area, Ti is associated with Nb and/or (Nb + Ta), elements that act as quenchers of cathodoluminescence, so that CL intensity prediction is difficult if not impossible. A general observation is that luminescence in the range of 330-660 nm clearly decreases with increase of the Nb and Ta concentration.

Contribution of RISE Confocal Raman imaging integrated in a SEM

Raman spectroscopy provides qualitative information on the presence and distribution of trace elements in cassiterite, based on the presence, intensity, and position of Raman bands. The characteristic Raman bands for SnO_2 are the A_{1G} band at 638 rel. 1/cm and B_{1G} band at 741 rel. 1/cm (figure 7b). They correspond to the symmetric and asymmetric stretching of the Sn-O bonds respectively. Upon incorporation of different elements in the crystal lattice, shifts, broadenings and the appearance of additional Raman bands in the Raman spectrum will occur. According to Wang and co-authors (Wang et al., 1993), a variation of several peaks in Raman shift intensity is observed for the trace element ratio (Nb + Ta)/(Fe + Mn).

The primary problem for Raman analysis on such a cassiterite grain is related to the location of the region of interest, which cannot be analyzed - or at least not easily - by optical microscopy. As a result, SEM SE (secondary electrons), BSE (backscattered

electrons), and CL imaging were used to determine the precise location of the area of interest (mainly based on the co-location of cracks in the selected area). After locating the region of interest, the sample was transferred inside the vacuum chamber to the confocal Raman measuring position for further analysis. A Raman image (200x200 μm^2) was collected from the region of interest, by acquiring a 2D array of 200x200 complete Raman spectra with an integration time of 0.08s per spectrum. The total acquisition time for the Raman image consisting of 40000 spectra was 53 minutes. The 2D array of Raman spectra was analyzed with multivariate spectral analysis methods such as Cluster Analysis, described in details by T. Dieing and W. Ibach (Dieng & Ibach, 2010) The Raman spectra obtained from these analysis are presented in Figure 7a. All four spectra contain the main A_{1G} band at 638 rel.1/cm indicating the presence of SnO_2 in the analyzed crystal. The distribution of the four components in the analyzed sample area is presented in the color coded Raman image (Figure 7a). The colors in the Raman image match the colors of the Raman spectra. As shown previously, based on EBSD and EPMA analyses, this part of the grain is characterized by different areas including main/twin crystal orientation and high/low trace element concentrations. The overlay of the Raman image with the CL image (Figure 7a) highlights the sensitivity of Raman spectroscopy to grain orientation and incorporation of trace elements in the crystal structure of SnO_2.

Beside the SnO_2 characteristic Raman bands, the spectrum in Figure 7b (spectrum d) contains a Raman band at 840 rel. 1/cm which can be associated to the A_n vibrational mode of Nb (Wang et al., 1993). By comparing the Raman image (Figure 7a) with the elemental distribution of Nb (Figure 6b), a clear correlation can be made. On the other hand, the A_n band is weak or not visible on the green and purple spectra (figure 7b spectra a and c), those corresponding to a low Nb content. Low Nb

coupled with a low Ti concentration is observed for the purple area (figure 7a and figure 7b spectrum a), and low Nb coupled with a high Ti concentration is noted for the green area (figure 7a and figure 7b spectrum c). The B_{2g} band at 741 1/cm is strong on the purple spectrum (figure 7b spectrum a) and quite weak on the green one (figure 7b spectrum c). The intensity of this band is high compared to the A_n band when characterized by a medium to high Nb content associated with Ta (± Fe) and a low Ti content (purple and blue spectra - figure 7b spectra a and d). In the opposite case, the intensity of the B_{2g} band is low compared to the A_n band when Nb and Ta contents are low and Ti is high (green spectrum - figure 7b spectrum c). According to Izoret et al (Izoret et al., 1985), the substitution Sn – Ti in cassiterite is isomorphic and homovalent (Sn^{4+} / Ti^{4+}) whereas at the other end, the Sn – (Nb,Ta) substitution is heterovalent (Sn^{4+} / Nb^{5+},Ta^{5+}) with the necessity of local charge compensation (for example with Fe^{3+}).

In addition, according to EPMA map of tungsten W (data not shown), the blue spectrum (figure 7b spectrum b) could be attributed to wolframite.

Thus a relationship can be established between these Raman spectral differences and trace element contents, which agree with the conclusions of Wang and co-authors (Wang et al., 1993). RISE imaging enables a direct link of Raman spectra to trace element distribution and crystal orientation at the micrometric / sub-micrometric scale in SnO_2 minerals.

CONCLUSION

In this study, cassiterite zonation and orientation was explored using a panel of SEM-based imaging and microanalysis techniques. The panchromatic intensity of cathodoluminescence of a cassiterite grain is affected by both crystal orientation and

trace element distribution. The correlation of CL intensity with crystallographic orientation (EBSD) and trace element distribution (EPMA) can be clearly identified and the influence of each element can be defined at the micrometric scale. The influence of trace elements on luminescence intensity is clearly established.

In addition, we present the benefits of using confocal Raman imaging integrated in a SEM (RISE microscopy). Cassiterite grain analyses on the same area show the complementarity between the various analyses and observations performed by SEM-CL imaging, crystallographic observations (EBSD), elemental analyses and trace element distribution (EPMA), and confocal Raman spectroscopy / imaging. The advantage of using RISE imaging and spectroscopy at a sub-micrometric scale has been highlighted because of its ability to detect, discriminate, and characterize sub-micrometric areas and phases present in a complex cassiterite grain (down to less than 400nm according to Jiruse et al., 2014), in correlation with trace elements and crystallographic orientation. The presence of Ta and Nb (heterovalent substitution) correlates with increased A_n (~ 840 1/cm) and B_{2g} (~ 741 1/cm) band intensities, whereas the Raman spectrum of an area with a low Nb and Ta coupled with a high Ti content (homovalent substitution) appears to exhibit low intensity A_n and B_{2g} bands. The combination of data collected from the different techniques makes it possible to link directly both chemical and crystallographic data and the changes in the Raman spectrum of cassiterite.

370 References

371

372 Autrata R. (1992) Single crystal detector suitable for high resolution scanning
373 electron microscopy, EMSA Bulletin 22, 54-58

374 Ballevre M., Le Goff E., Hebert R. (2001) The tectonothermal evolution of the
375 Cadomian belt of northern Britanny, France: a Neoproterozoic volcanic arc.
376 Tectonophysics 331, 19-43

377 Botelho N.F., Moura M.A. (1998) Granite-ore deposit relationships in Central Brazil,
378 Journal of South American Earth Sciences. 11(5), 427 – 438.

379 Briskey J.A. (2005) Indium in Zinc-Lead and Other Mineral Deposits, A
380 Reconnaissance Survey of 1118 Indium analyses published before 1985, U.S.
381 Geological Survey Open-File Report, 2005-1209

382 Cerny P., Roberts W.L., Ercit T.S., & Chapman, R. (1985) Wodginite and associated
383 oxide minerals from the Peerless pegmatite, Pennington County, South Dakota,
384 American Mineralogist, 70, 1044-1049.

385 Chauris L., Lulzac Y., Cotten J. (1989) Une lame de granite albitique tardi-
386 cadomienne : le gisement stanno-wolframifère de Montbelleux (Massif armoricain,
387 France), Chronique de la recherche minière., 496, 25-39

388 Das S., Hendry M.J. (2011) Application of Raman spectroscopy to identify Iron
389 minerals commonly found in mine waste. Chemical Geology 290, 101-108

390 Dieing T. and Ibach W. (2010) Software Requirements and Data Analysis in
391 Confocal Raman Microscopy. Springer Series in Optical Sciences 158, Editors Dieing
392 T., Hollricher O. and Toporski J.

393 Everhart T.E., Thornley R.F.M. (1960) Wide-band detector for micro-microampere
394 low-energy electron currents, Journal of Scientific Instruments, 37, 246.

Farmer C.B., Searl A., Halls C. (1991) Cathodoluminescence and growth of cassiterite in the composite lodes at south Corfty Mine, Cornwall, England. Mineralogical magazine 55, 447-458

Gao T., Fjellvag H., Norby P. (2009) A comparison study of Raman scattering properties of α- and β-MnO_2. Analytica Chimica Acta 648, 235-239

Giuliani G. (1987) La cassitérite zonée du gisement de Sokhret Allal (Granite des Zaër; Maroc Central): Composition chimique et phases fluides associées, Mineralium deposita 22, 253 – 261

Hall A.J. (1978) Post-Growth Readjustment of a Cassiterite Twin-Boundary Revealed by Cathodoluminescence, Mineralogical Magazine 42, 288-290

Hall, M.R., Ribbe, P.H. (1971) An electron microprobe study of luminescence centers in cassiterite, American Mineralogist, 56, 31-45.

Hope G.A., Wood R., Munce C.G. (2001) Raman microprobe mineral identification, Mineral Engineering, 14 (12), 1565-1577

Izoret L., Marnier G., Dusausoy Y. (1985) Caracterisation cristallochimique de la cassiterite des gisements d'etain et de tungstene de Galice, Espagne, Canadian Mineralogist, 23, 221-231

Jacka M., Zadrazil M., Lopour F. (2003) A differentially pumped secondary electron detector for low-vacuum scanning electron microscopy, Scanning 25, 243-246.

Jarvis R.M., Brooker A., Goodacre R. (2004) Surface-enhanced Raman spectroscopy for bacterial discrimination utilizing a scanning electron microscope with a Raman spectroscopy interface, Analytical Chemistry, 76, 5198-5202

Jarvis R.M., Goodacre R. (2004) Discrimination of bacteria using surface-enhanced Raman spectroscopy, Analytical Chemistry 76, 40-47

419 Jiruše J., Haničinec M., Havelka M., Hollricher O., Ibach W., Spizig P. (2014)
420 Integrating focused ion beam–scanning electron microscope with confocal Raman
421 microscope into a single instrument, Journal of Vacuum Science & Technology B, 32,
422 06FC03
423 Lahfid A., Beyssac O., Deville E., Negro F.,Chopin C., Goffé B. (2010) Evolution of
424 the Raman spectrum of carbonaceous material in low-grade metasediments of the
425 Glarus Alps (Switzerland). Terra Nova 22, 354–360
426 Lerouge C., Deschamps Y., Piantone P., Gilles C., Breton J. (2007) Metal-carrier
427 accessory minerals associated with W ± Sn mineralization, La Châtaigneraie
428 tungsten ore district, Massif Central, France. Canadian Mineralogist 45, 875–889
429 Lerouge C., Gloaguen E., Wille G., Bailly L. (2017) The distribution of In and other
430 rare metals in cassiterite and associated minerals in Sn ± W ore deposits of the
431 Western Variscan Belt, European Journal of Mineralogy (accepted)
432 Lloyd G.E. (1987) Atomic number and crystallographic contrast images with the SEM,
433 a review of backscattered electron techniques, Mineralogical Magazine 51, 3 - 19
434 Maubec N., Lerouge C., Lahfid A., Wille G., Michel K., Bourrat X. (2013) Coupled
435 SEM-microRaman system: A powerful tool to characterize a micrometric aluminum-
436 phosphate–sulfate (APS) - Journal of Molecular Structure 1048, 33–40
437 Möller P., Dulski P., Szacki W., Malow G., Riedel E. (1988) Substitution of tin in
438 cassiterite by tantalum, niobium, tungsten, iron and manganese. Geochimica
439 Cosmochimica Acta 52, 1497-1503
440 Mossbrucker J., Grotjohn T.A. (1996) Determination of local crystal orientation of
441 diamond using polarized raman spectra. Diamond and Related Materials 5, 1333-
442 1343

Mossbrucker J., Grotjohn T.A. (1997) Determination of the components of stress in a polycrystalline diamond film using polarized Raman spectroscopy. Journal of Vacuum Science and Technology A: Vacuum, Surfaces and Films 15 (3), 1206

Murciego A., Garcia Sanchez A., Dusausoy Y., Martin Pozas J. M., Ruck R. (1997) Geochemistry and EPR of cassiterite from the Iberian Hercynian Massif., Mineralogical Magazine 61(3), 357-365.

Neiva, A.M.R. (1996) Geochemistry of cassiterite and its inclusions and exsolution products from tin and tungsten deposits in Portugal. 34, 745 - 768

Nelson M.P., Zugates C.T., Treado P.J., Casuccio G.S., Exline D.L., Schlaegle S.F. (2001) Combining Raman Chemical Imaging and Scanning Electron Microscopy to Characterize Ambient Fine Particulate Matter, Aerosol Science and Technology 34, 108-117.

Nespolo M., Souvignier B. (2015) Structural rationale for the occurrence of the elbow twins in cassiterite and rutile, Journal of Mineralogical and Petrological Sciences 110, 157-165

Otieno-Alego V. (2009) Some forensic applications of a combined micro-Raman and scanning electron microscopy system, Journal of Raman Spectroscopy 40, 948-953

Pointurier F., Marie O. (2010) Identification of the chemical forms of uranium compounds in micrometer-size particles by means of micro-Raman spectrometry and scanning electron microscope, Spectrochimica Acta Part B-Atomic Spectroscopy 65, 797-804.

Remond G., Cesbron F., Chapoulie R., Ohnenstetter D., Roques-Carmes C., Schvoerer M. (1992) Cathodoluminescence applied to the microcharacterization of mineral materials ; a present status in experimentation and interpretation, Scanning Microscopy 6(1), 23-68

Remond, G. (1973) Exemples d'identification et de localisation des elements en traces dans les minéraux luminescents (cassiterites), à l'aide de l'analyseur ionique. Bulletin de la Societe francaise de Mineralogie et de Cristallographie 96, 183-198.

Rossi P., Cocherie A., Meyer G., Fouillac A.M. Autran A. (1988) Metallogenic W and Sn granites: Genesis and main distinguishing features. In: Boissonnas J., Omenetto P. (eds) Mineral Deposits within the European Community. Special Publication No. 6 of the Society for Geology Applied to Mineral Deposits, vol 6. Springer, Berlin, Heidelberg

Serranti S., Ferrini V., Masi U., Cabri L.J. (2002) Trace-element distribution in cassiterite and sulfides from rubané and massive ores of the Corvo deposit, Portugal, Canadian Mineralogist 40, 815-835

Stefaniak, E.A., Alsecz, A., Frost, R., Mathe, Z., Sajo, I.E., Torok, S., Worobiec, A., VanGrieken, R. (2009) Combined SEM/EDX and micro-Raman spectroscopy analysis of uranium minerals from a former uranium mine, Journal of Hazardous Materials 168 (1), 416–423

Stefaniak, E.A., Pointurier, F., Marie, O., Truyens, J., Aregbe, Y., (2014) In-SEM Raman microspectroscopy coupled with EDX--a case study of uranium reference particles, Analyst 139 (3), 668–675

Van Apeldoorn A.A., Aksenov Y., Stigter M., Hofland I., De Bruijn J.D., Koerten H.K.,Otto C., Greve J., Van Blitterswijk C.A. (2005) Parallel high-resolution confocal Raman SEM analysis of inorganic and organic bone matrix constituents, Journal of The Royal Society Interface 2 (2), 39–45

Wang R., Wu J., Dubessy J., Monchoux P. (1993) Raman Spectroscopy of Nb, Ta-rich Cassiterite in Beauvoir and Montebras Granites, France – Chinese Journal of Geochemistry 12(4), 353–360

493 Wille G., Bourrat X., Maubec N., Lahfid A. (2014) Raman-in-SEM, a multimodal and
494 multiscale analytical tool: performance for materials and expertise, Micron 67, 50-64
495 Worobiec A., Potgieter-Vermaak S., Brooker A., Darchuk L., Stefaniak E.,
496 VanGrieken R. (2010) Interfaced SEM/EDX and micro-Raman Spectrometry for
497 characterisation of heterogeneous environmental particles — Fundamental and
498 practical challenges, R., Microchemical Journal. 94 (1), 65–72
499

Tables

Table 1: Average contents of main trace elements in cassiterite from Montbelleux by EPMA (after Lerouge et al. 2007).

Table 2: Average contents of main trace elements in the different area identified by RISE microscopy (from EPMA analysis). Detection limit for each element is given in brackets

Figures

Figure 1: Location of Montbelleux deposit and SEM (BSE) images of the cassiterite surrounding minerals (after Lerouge et al. 2017).

Figure 2: SEM – panchromatic cathodoluminescence image of a centimetric cassiterite grain (red arrow: position of analyzed area – see figure 3)

Figure 3: Secondary electrons (a) and panchromatic cathodoluminescence (b) images of the Cassiterite grain area

Figure 4: EBSD orientation map of the area of interest (a), CL image (b), and [001] inverse pole figure (c)

Figure 5: WDS interference Ta Mα / Sn Lα (2nd order) on a TAP monochromator

Figure 6: comparison of cathodoluminescence image (CL) (a) and RISE imaging map (b) with elemental mapping for trace elements Ta (c), Nb (d), Fe (e) and Ti (f) –. Fissures are indicated in red. White lines give limits of small domains presenting different orientations of growth and low luminescence.

Figure 7: Raman map superimposed on CL image (a) and Raman spectrum of each area identified on the Raman map (b) - average content of trace elements in areas identified by Raman imaging (c - see Table 2) expressed in atom per formula unit (a.p.f.u) for the understanding of the substitution in the mineral.

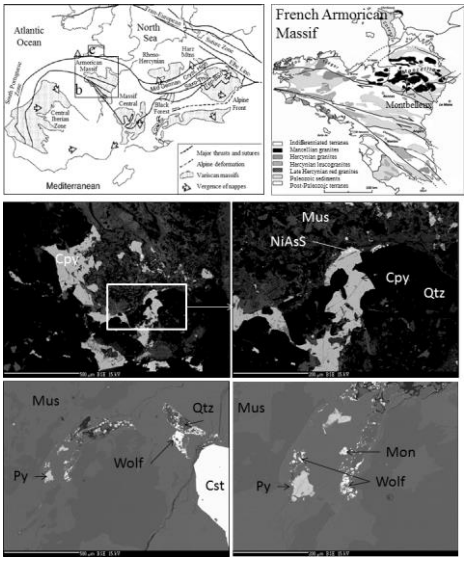

525

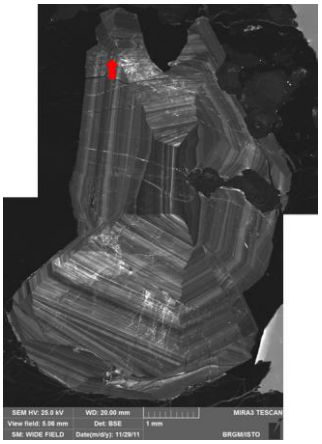

526

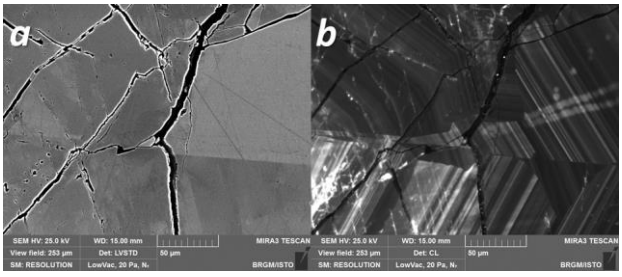

527

528

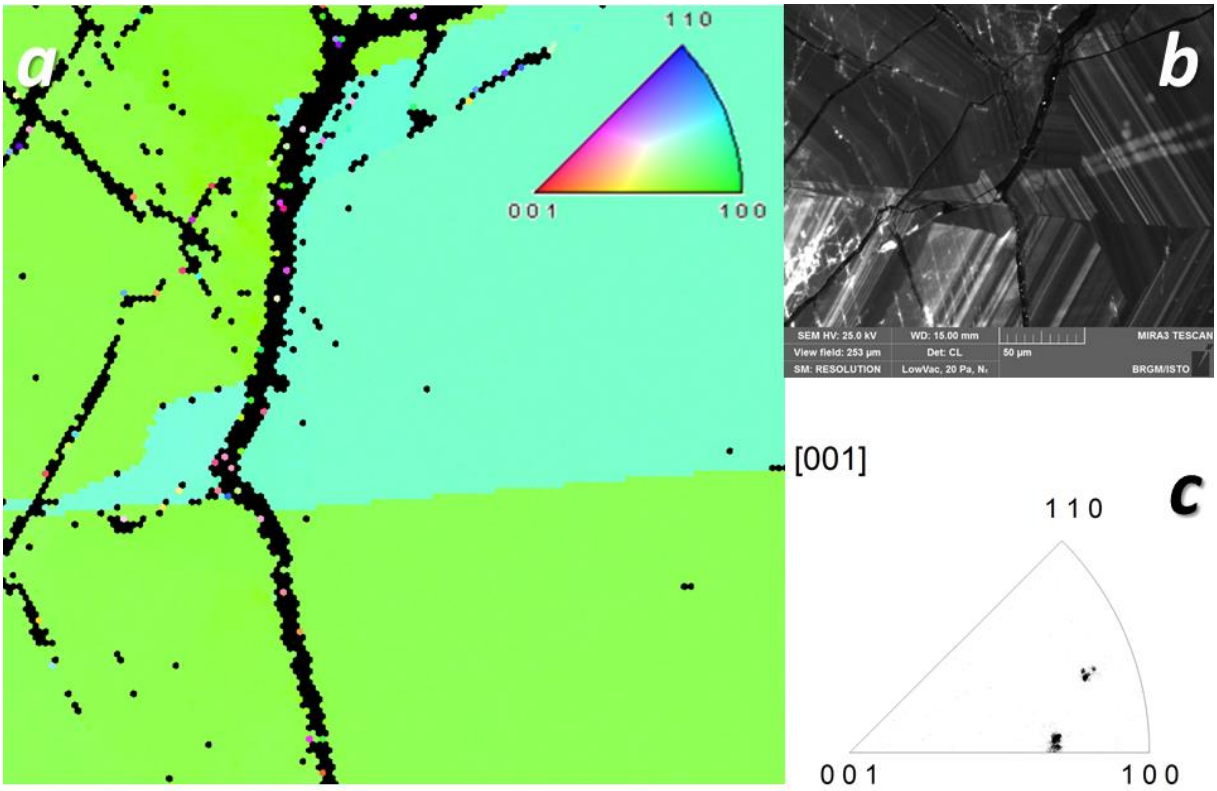
a
110
001
100
b
SEM HV: 25.0 kV
WD: 15.00 mm
MIRA3 TESCAN
View field: 253 µm
Det: CL
50 µm
SM: RESOLUTION
LowVac, 20 Pa, N2
BRGM/ISTO
[001]
c
110
001
100

529

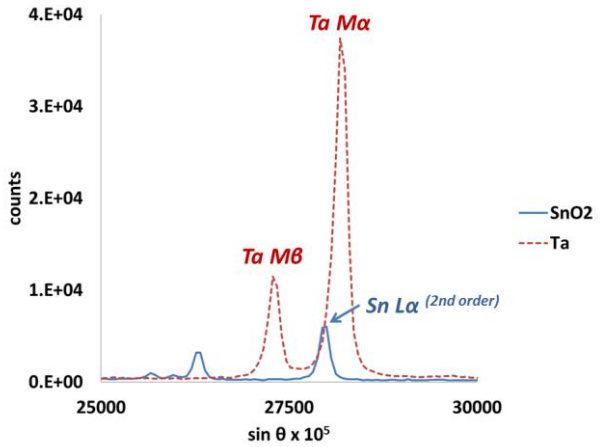
4.E+04
3.E+04
2.E+04
1.E+04
0.E+00
counts
Ta Mα
Ta Mβ
Sn Lα (2nd order)
SnO2
Ta
25000
27500
30000
sin θ x 10^5

530

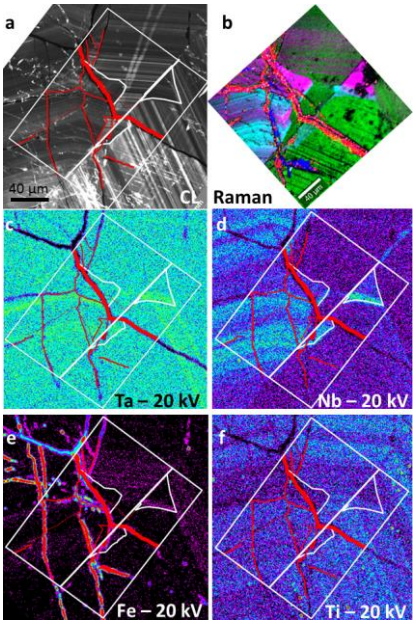

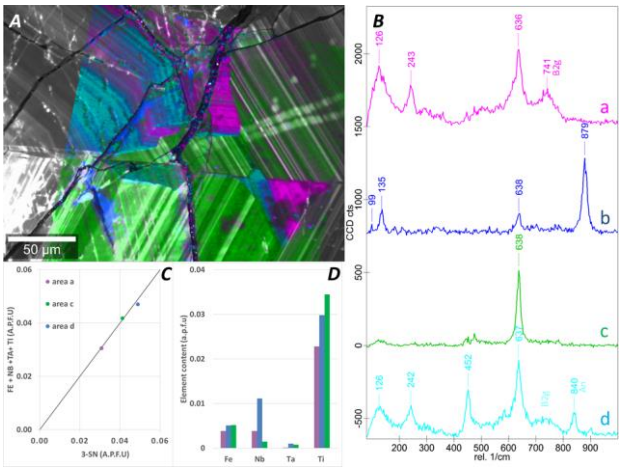

Table 1: Average contents of main trace elements in cassiterite from Montbelleux by EPMA (after Lerouge et al. 2007).

number of analyses		SnO_2 wt %	Trace element contents ($mg.kg^{-1}$)				
			Fe	In	Nb	Ta	Ti
45	average	98.97	2568	519	3901	5809	2635
	std. dev.	0.74	1402	204	3487	4325	1377

$Sn_{2.92\pm0.04}$ $Fe_{0.02\pm0.01}$ $Nb_{0.02\pm0.02}$ $Ta_{0.01\pm0.01}$ $Ti_{0.02\pm0.01}$ O_2

539 Table 2: Average contents of main trace elements in the different area identified by
540 RISE microscopy (from EPMA analyses). Detection limit (in %) for each element is
541 given in brackets

542

Area	TiO_2 *(0.03)*	FeO *(0.035)*	Nb_2O_5 *(0.018)*	SnO_2 *(0.163)*	Ta_2O_5 *(0.050)*
a	0.405	0.061	0.114	99.413	0.000
c	0.612	0.083	0.043	99.223	0.000
d	0.531	0.082	0.329	99.009	0.050

543
544